

Evidence of a structural phase transition in the triangular-lattice compound CuIr_2Te_4

H. C. Wu,^{1,2,*} Y. C. Chung,¹ T. W. Yen,¹ H. J. Chen,¹ T. W. Kuo,¹ D. Chandrasekhar Kakarla,^{1,2} S. M. Huang,¹ Y.-Y. Wang,³ J.-Y. Lin,^{3,4} J. J. Lee,⁵ Y. C. Lai,⁵ C. L. Chen,⁵ J. F. Lee,⁵ T. L. Chou,⁶ Y.-C. Lai,⁶ M.-W. Chu,⁶ Mitch M. C. Chou,² and H. D. Yang^{1,2,†}

¹Department of Physics, National Sun Yat-sen University, Kaohsiung 804, Taiwan


²Center of Crystal Research, National Sun Yat-sen University, Kaohsiung 804, Taiwan

³Institute of Physics, National Chiao Tung University, Hsinchu 30010, Taiwan

⁴Center for Emergent Functional Matter Science, National Chiao Tung University, Hsinchu 30010, Taiwan

⁵National Synchrotron Radiation Research Center, Hsinchu 30076, Taiwan

⁶Center for Condensed Matter Sciences, National Taiwan University, Taipei 10617, Taiwan

 (Received 24 November 2020; revised 17 March 2021; accepted 18 March 2021; published 29 March 2021)

Synthesized $\text{CuIr}_2(\text{Te}_{1-x}\text{Se}_x)_4$ samples were comprehensively characterized using various techniques. At ambient pressure, CuIr_2Te_4 undergoes an anomalous phase transition at $T_s \sim 250$ K with a large thermal hysteresis of $\Delta T_s \sim 40$ K and a superconducting transition at $T_c \sim 3$ K during magnetization and electrical-resistivity measurements. We determined this transition to be a first-order structural phase transition from high-temperature hexagonal ($P\bar{3}m1$) to low-temperature triclinic ($P\bar{1}$) symmetry. Both external physical pressure and chemical doping largely enhance T_s and ΔT_s and suppress T_c , thereby indicating a strong correlation between T_s and T_c . Critically, no superlattice is observed below T_s as per the electron-diffraction examinations. Thus, the anomalous phase transition at T_s , which exhibits a large thermal hysteresis in resistivity and magnetization measurements, is structural rather than a charge-density-wave formation.

DOI: [10.1103/PhysRevB.103.104111](https://doi.org/10.1103/PhysRevB.103.104111)

I. INTRODUCTION

The competition and correlation between structural, electronic, charge, and spin orderings have attracted significant research interest in the realm of condensed-matter physics. In this context, the well-known phenomenon of charge-density-wave (CDW) instability observed in low-dimensional crystallographic structures [1–3] or quasi-one-dimensional chains [4–6] has been reported to originate from the strongly anisotropic topology related to Fermi-surface nesting. In the single-phase material [7–10], the CDW state has been extensively studied, along with other physical properties such as magnetism and superconductivity (SC), via comprehensive experimental observations and theoretical calculations. Key experimental tools utilizing high pressure [11], chemical substitution [12], or intercalation [13] effects are crucial to obtain insight into the competition between CDW and SC (or magnetic) orderings.

Meanwhile, three-dimensional (3D) rare-earth transition-metal ternary silicides such as $\text{Sc}_5\text{Co}_4\text{Si}_{10}$ (space group, $P4/m\bar{b}m$) and $\text{U}_2\text{Co}_3\text{Si}_5$ (space group, $Ibam$) have been classified under the CDW family [14–16]. Fundamentally, the conventional second-order CDW transition is substantially driven by the electronic entropy effect [14]. However, an unambiguous thermal hysteresis loop close to the CDW transition has been observed in $\text{Lu}_2\text{Ir}_3\text{Si}_5$ (~ 40 K) [16] and

$\text{Lu}_5\text{Rh}_4\text{Si}_{10}$ (~ 2 K) [17], thereby indicating the coexistence of the structural phase transition and CDW instability in CDW materials. To advance related research, it is necessary to simultaneously study the crystal structure and microelectron diffraction around the critical temperature (T) to verify potential CDW materials.

The compound CuIr_2Te_4 is classified as a $\text{Cu}M_2X_4$ system, wherein M denotes a transition metal (Rh, Ir) and X is a chalcogen (O, S, Se, Te) [18–26]. In contrast to the normal cubic spinel ($Fd\bar{3}m$) structure of the space group of CuIr_2X_4 ($X = \text{S, Se}$), CuIr_2Te_4 exhibits a low-dimensional crystal structure (defect NiAs structure) [18] with the disordered trigonal symmetry of space group $P\bar{3}m1$, as shown in Fig. S1 of the Supplemental Material [27]. CuIr_2S_4 with an ionic configuration of $\text{Cu}^+\text{Ir}^{3+}\text{Ir}^{4+}\text{S}_4^{2-}$ [20,21] undergoes a first-order metal-insulator transition (MIT) [20,21] along with orbital-induced Peierls-like phase transition [22] near 226 K, whereas CuIr_2Se_4 exhibits a metallic behavior down to 0.4 K without T_c or MIT [26]. Recently, CDW was reported in the quasi-two-dimensional (Q2D) telluride chalcogenide superconductor CuIr_2Te_4 [18,19] based on the observed anomalous phase transition with a large hysteresis loop near 250 K in resistivity and magnetization measurements. However, thus far, there is no direct microscopic evidence of CDW superlattices in CuIr_2Te_4 . This situation motivated us to further explore the origin of the anomalous transition using synchrotron x-ray powder diffraction (SXRPD) and selected area electron diffraction (SAED). In this paper, we focus on the following aspects: (1) the origin of the high- T anomalous phase transition via T -dependent structural, magnetic, and transport

*Corresponding author: hungcheng.wu@g-mail.nsysu.edu.tw

†Corresponding author: yang@mail.nsysu.edu.tw

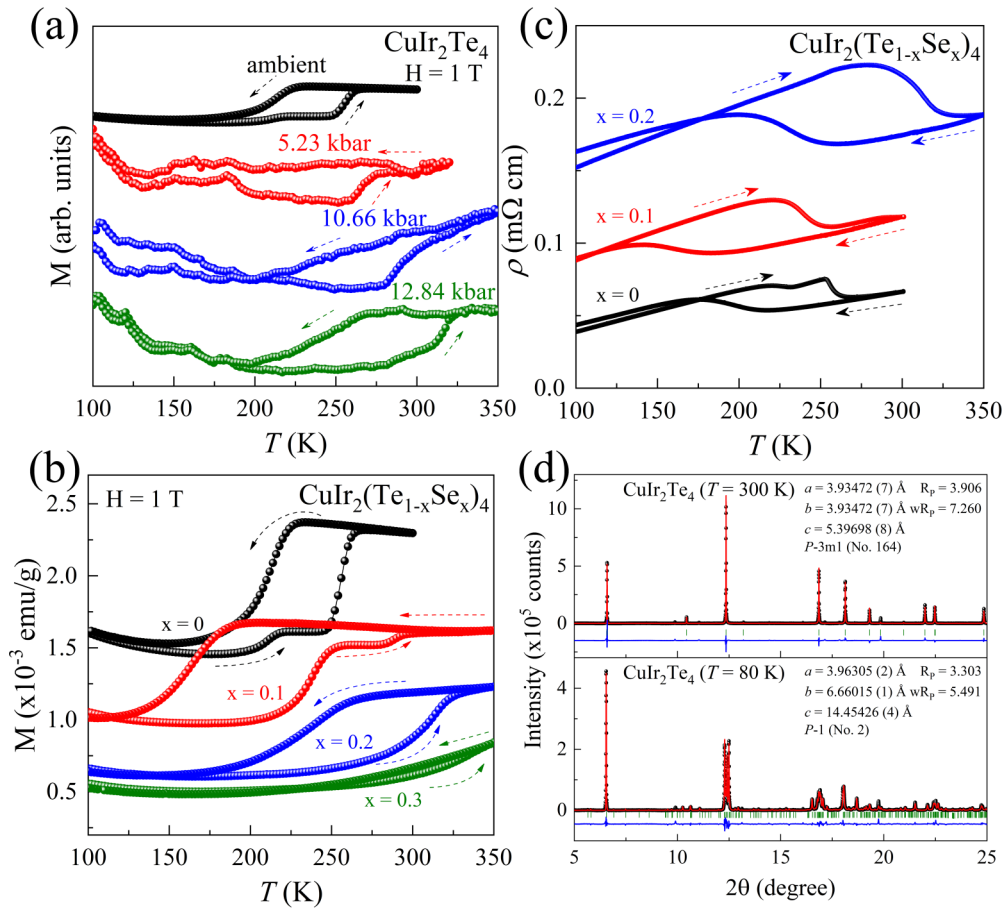


FIG. 1. Pressure (P) and chemical-substitution effects on high- T anomalous phase transition in polycrystalline CuIr_2Te_4 . (a) Temperature-dependent magnetization measurements of CuIr_2Te_4 under several applied P values up to 12.84 kbar, acquired during heating and cooling cycles from 105 to 350 K. Temperature dependent (b) magnetization and (c) electrical-resistivity curves of $\text{CuIr}_2(\text{Te}_{1-x}\text{Se}_x)_4$. (d) The Rietveld-refined SXRPD patterns of CuIr_2Te_4 at 300 K (high- T phase, $P\bar{3}m1$) and 80 K (low- T phase, $P\bar{1}$), which confirm the occurrence of a structural phase transition.

measurements; (2) the effects of physical pressure (P) and chemical substitution (Se doping at Te sites) on the crystal structure and anomalous transition; (3) the observation of a possible superlattice based on SAED and electronic instability via x-ray absorption near-edge structure (XANES) and extended x-ray absorption fine structure (EXAFS) investigations.

II. EXPERIMENTAL METHODS

Polycrystalline samples of $\text{CuIr}_2(\text{Te}_{1-x}\text{Se}_x)_4$ ($0 \leq x \leq 0.3$) were synthesized via the conventional solid-state reaction method [18]. Stoichiometric mixtures of high-purity Cu, Ir, Te, and Se powders were pressed into pellets, sealed in an evacuated quartz tube, and heated to 850 °C at a heating rate of 30 °C/h; the temperature was maintained at 850 °C for 96 h, and the pellets were eventually naturally cooled to room temperature (RT) by switching off the furnace. The T -dependent synchrotron x-ray powder diffraction patterns were acquired at the TPS 09A (20 keV) and TLS-01C2 (14 keV) beamlines with full width at half maximum (FWHM) of 0.01° and 0.07° at 2θ , respectively, at the National Synchrotron Radiation Research Center (NSRRC) in Hsinchu, Taiwan. For low- T measurement at the TPS 09A, the data

were collected using the MYTHEN 24K microstrip x-ray detector and the Cryostream Cooler system was used for the temperature range of 80–300 K. For high- T measurement at the TLS-01C2, the MAR345 image plate detector was used for collecting the data and a hot air gas blower system was equipped to control the temperature from 300 to 460 K. The obtained data were further refined using the EXPO 2014 software. The room temperature SXRPD measurement was performed with a photon energy of 20.5 keV under P by using a diamond anvil cell (DAC) at the TLS-01C2 beamline as per the experimental procedure [28]. The chamber in the DAC containing the powdered CuIr_2Te_4 sample and a small amount of ruby powder was sealed by using silicone oil as a pressure transmitting fluid (Alfa Aesar, polydimethylsiloxane, trimethylsiloxy terminated, M.W. 410). The ruby R1 fluorescence spectra obtained using the Raman spectrometer iHR550 (Horiba Jobin Yvon) were recorded to determine the pressure in DAC. A piston-cylinder-type BeCu pressure cell designed for the MPMS-XL7 magnetic property measurement system (Quantum Design), in which the Daphne-7373 oil was used as a pressure transmitting fluid, was used for the P -dependent DC magnetization measurements. The *in situ* pressure in the BeCu pressure cell was determined with a superconducting

lead manometer. The T -dependent electrical-resistivity measurements were conducted by using the conventional DC four-probe method. T -dependent XANES and EXAFS were performed in the fluorescence mode at the TLS-17C1 beamline. A double-crystal Si(111) monochromator was used to ensure the measured energy resolution was better than 1.4 eV. A JEOL 2000 FX transmission electron microscope (200 kV) equipped with a low- T sample holder was employed to obtain the SAED patterns. The input parameters of lattice constants, atomic positions, and the space group symmetry ($P\bar{3}m1$) retrieved from SXRD experiments were used for *ab initio* calculations of CuIr_2Te_4 by using the VASP program (version 5.4.4). The basis sets for Cu, Ir, and Te atoms were derived using the projector-augmented plane wave (PAW) method and a cutoff value of 400 eV was set. Furthermore, the exchange-correlation functional was generalized gradient approximation–Perdew–Burke–Ernzerhof. The PSTRESS tag was included in the VASP script to simulate a hydrostatic pressure on CuIr_2Te_4 . We then relaxed the $P\bar{3}m1$ unit cell in terms of its total volume, cell shape, and atomic positions until it reached the convergence criterion, i.e., the change in total energy between two ionic steps was less than 10^{-4} . At the prescribed pressure, the relaxed lattice constants and the corresponding total (free) converged energy were collected for further analysis and discussions.

III. RESULTS AND DISCUSSION

A. Pressure and chemical substitution effects on high- T anomalous phase transition in CuIr_2Te_4

At ambient P , Fig. 1(a) shows the zero-field-cooled (ZFC) and field-cooled (FC) magnetization curves of CuIr_2Te_4 at 1 T with a large thermal hysteresis (ΔT_s); these results are consistent with previous reports [18,19]. Under external P , the ΔT_s loop increases in size and systematically shifts to high T values for P values up to 12.84 kbar. On other hand, the ΔT_s loop shown in Fig. 1(b) also exhibits a similar shift to higher T values with higher Se doping. For $x = 0.3$, the exact ΔT_s may be above 350 K. Our comparison of the effects of hydrostatic P and chemical substitution (Se doping) on ΔT_s indicates that both these factors similarly affect the high- T anomalous phase transition. Figure 1(c) represents the T -dependent electrical-resistivity curves during the heating and cooling cycle for $x = 0, 0.1$, and 0.2 . For $x = 0.3$, the sample is powderlike, which leads to practical difficulties in conducting transport measurements. We observe that ΔT_s shifts to higher T values with increasing x ; this result is consistent with that observed in Fig. 1(b). According to Refs. [18,19], the ΔT_s enhancement is possibly due to the CDW instability. However, CDW behavior corresponds to second-order transition characteristics, and it is significantly suppressed by perturbation factors such as P and chemical doping [11,29]. The significant hysteresis observed in Figs. 1(a)–1(c) unambiguously suggests the first-order nature of the transition. Thus, the transition at T_s probably represents a structural phase transition rather than a change in CDW. To explore the existence of a possible low- T phase in CuIr_2Te_4 , we acquired the SXRPD patterns at 300 and 80 K, as shown in Fig. 1(d). Interestingly, the 80 K pattern completely differs from that obtained at 300 K.

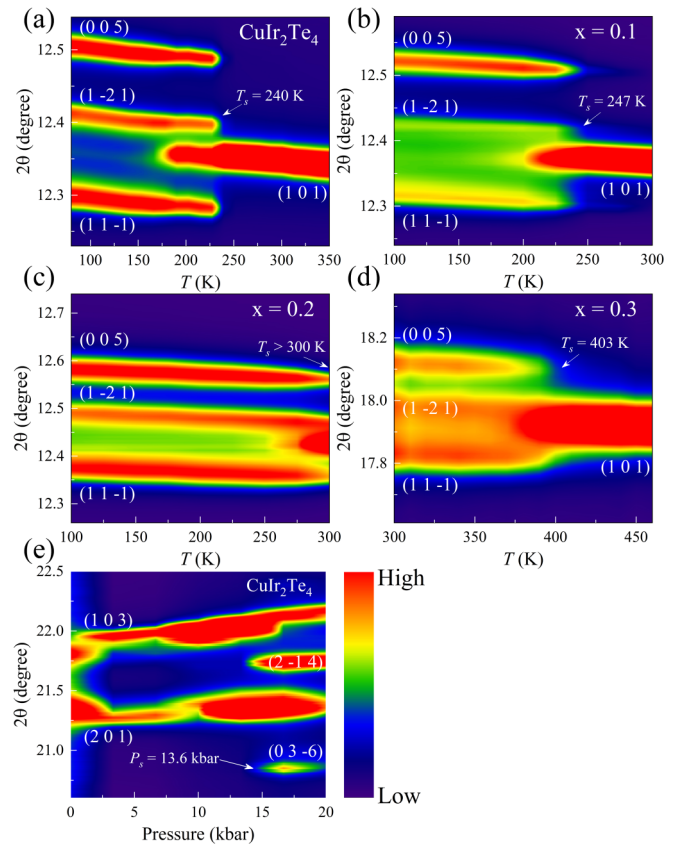


FIG. 2. (a)–(d) SXRPD evolution as a function of T in $\text{CuIr}_2(\text{Te}_{1-x}\text{Se}_x)_4$. The structural phase transition (T_s) systematically shifts to higher T values with increasing Se concentration. (e) Pressure (P)-dependent SXRPD spectra of CuIr_2Te_4 at 300 K. A P -enhanced structural transition (P_s) from the high- T hexagonal $P\bar{3}m1$ phase to the low- T triclinic $P\bar{1}$ phase is observed above 13.6 kbar.

After careful Rietveld refinement, all the Bragg reflections at 80 K can be indexed to the triclinic structure with space group $P\bar{1}$ (no. 2). The obtained lattice constants and R -factor values are presented in Fig. 1(d), and the crystallographic data at 300 and 80 K are summarized in Table S1 of the Supplemental Material [27]. In addition, the SXRPD patterns with Rietveld refinements for $x = 0.1$ at 100 K, $x = 0.2$ at 100 K, and $x = 0.3$ at 100 K were also shown in Fig. S2 [27]. These results clearly establish that the origin of the transition at $T_s \sim 250$ K is strongly correlated with the structural phase transition (T_s) from $P\bar{3}m1$ to $P\bar{1}$ symmetry.

Further we have analyzed critical exponents associated with the $P\bar{3}m1$ to $P\bar{1}$ structural phase transition. Critical exponent studies were proven to obtain insights into the correlation between the superlattice misfit strain at the layered structure and T_c in several superconducting heterostructure such as cuprates, pnictides, and diborides [30]. A quantitative power law $P = a \times (T_{\text{critical}}/T - 1)^\beta$ analysis has been carried out for the temperature dependent area of the (011) reflection peak shown in Fig. S3 [27]. The obtained critical exponent $\beta = 0.097$ in the present case is close to the predicted value for the two-dimensional Ising model ($\beta = 1/8$). A similar value

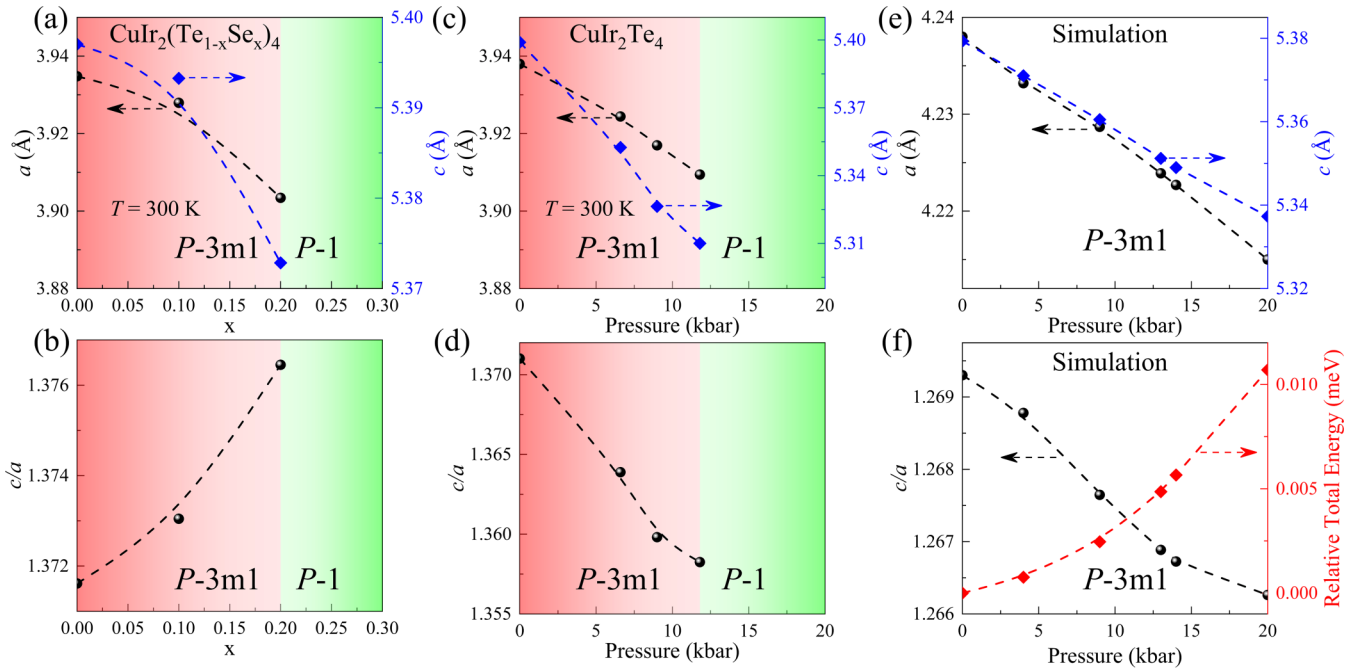


FIG. 3. Se-doping- and pressure (P)-dependent lattice parameters a and c and corresponding c/a ratios. The dashed lines serve as a visual guide. Variation in (a) lattice constants a (left axis) and c (right axis) and (b) c/a ratio for $\text{CuIr}_2(\text{Te}_{1-x}\text{Se}_x)_4$. Variation in (c) a (left axis) and c (right axis) and (d) c/a ratio of CuIr_2Te_4 under several applied pressures up to 20 kbar. (e) Simulation of constants a (left axis) and c (right axis) and (f) c/a ratio of CuIr_2Te_4 under high pressures from ambient pressure to 20 kbar. The relative total energy according to *ab initio* numerical calculations systemically increases under higher applied pressures, thereby suggesting that the crystal structure of $P\bar{3}m1$ in CuIr_2Te_4 becomes unstable under high pressure.

of the critical exponent was observed in the iron arsenides systems [31].

B. Chemical doping (Se) and pressure (P) dependent SXRPD patterns

To explore the T - and chemical-doping dependency of T_s in $\text{CuIr}_2(\text{Te}_{1-x}\text{Se}_x)_4$, we plotted the SXRPD evolution as a function of T for the $\text{CuIr}_2(\text{Te}_{1-x}\text{Se}_x)_4$ samples, as shown in Figs. 2(a)–2(d). All the patterns were acquired during the heating cycle in the T range of 100–300 K; only for the $x = 0.3$ sample, the T range was 300–460 K. These results show that T_s systematically shifts to higher T values with increase in the Se doping level. For $x = 0.3$, $T_s \sim 403$ K, and this value is consistent with the magnetization curve shown in Fig. 1(b). The detailed comparisons of the lattice parameters and c/a ratio at 300 K for $\text{CuIr}_2(\text{Te}_{1-x}\text{Se}_x)_4$ are presented in Fig. 3. The RT ΔT_s shown in Fig. 1(a) under P suggests the possibility of P -dependent structural phase transition in CuIr_2Te_4 . Thus, we acquired the P -dependent SXRPD patterns at 300 K, as shown in Fig. 2(e). We note that the initial reflection peaks persist when P is increased up to 13.6 kbar. The subsequent emergence of additional reflections ($P > 13.6$ kbar) indicates the breaking of crystal symmetry from the low- P hexagonal phase to the high- P triclinic phase. These results confirm that high P stabilizes the low- T triclinic phase at RT in CuIr_2Te_4 . Consequently, the initial T_s can be enhanced to RT under high P . To thoroughly examine how P or Se doping stabilizes the low- T triclinic phase, we obtained the RT structural quantities from the Rietveld-refined SXRPD patterns. At 300 K, param-

eters a and c decrease when x increases to 0.2 [Fig. 3(a)], whereas the c/a ratio increases [Fig. 3(b)]. Above $x = 0.2$, the crystal structure exhibits a triclinic phase, which indicates that Se doping stabilizes the low- T phase. Lattice constants a and c [Fig. 3(c)] also decrease with an increase in P up to 11.8 kbar. When $P > 11.8$ kbar, the triclinic phase is formed. In contrast to the Se-doping case, the c/a ratio [Fig. 3(d)] decreases with increasing P . The *ab initio* numerical calculations of CuIr_2Te_4 shown in Figs. 3(e) and 3(f) were computed with those obtained using VASP (version 5.4.4) to obtain the lattice constants and relative total energy under ambient and high- P conditions. These simulation results are consistent with the P -dependent SXRPD measurements. The higher relative total energy under P suggests that the high- T hexagonal phase becomes unstable, thus leading to the formation of the triclinic phase.

C. Correlation between structural phase transition and superconducting transition

To clarify the competition between T_s and the superconducting transition (T_c) in CuIr_2Te_4 , we performed magnetization measurements as a function of T under P [Fig. 4(a)]. The initial peak at $T_c \sim 3$ K under ambient condition shifts to lower T values with increasing P . Meanwhile, the diamagnetic-signal magnitude is almost completely suppressed at 12.84 kbar. Upon comparing the P and Se doping [Fig. 4(b)] effects, we note that T_c is initially constant and the diamagnetic-signal magnitude decreases at $x = 0.1$, and the T_c suddenly vanishes at $x = 0.2$. The phase diagrams of T vs P and T vs concentration x as plotted from the magnetization

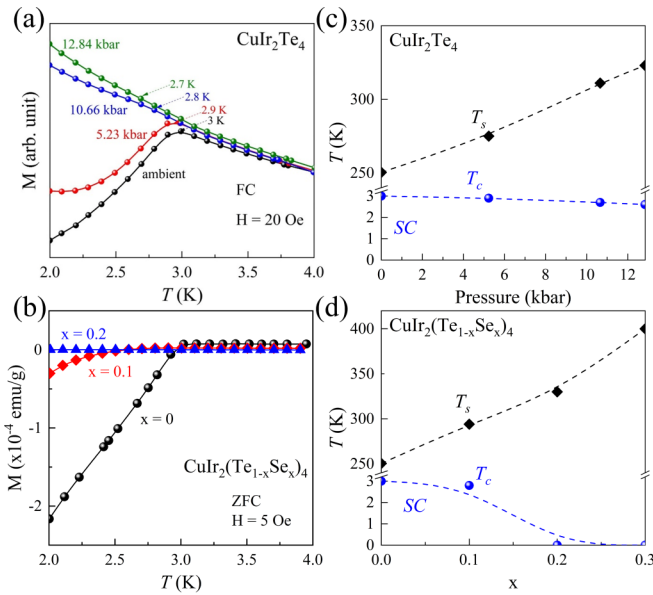


FIG. 4. Pressure (P) and chemical-substitution effects on low- T superconductivity transition in polycrystalline CuIr_2Te_4 . (a) P - and (b) Se-doping-dependent magnetization in the low T range from 2 to 4 K. Relationship between T_s and T_c as a function of (c) P and (d) Se doping. The dashed lines serve as a visual guide.

and SXRPD curves are summarized in Figs. 4(c) and 4(d); the physical P and chemical doping effects on T_c and T_s are similar in CuIr_2Te_4 .

D. Temperature-dependent SAED patterns

To further examine the CDW subtlety below T_s , we conducted SAED investigations at RT and 100 K (Fig. 5) while considering the superb capability of directly unveiling the related superperiodicity via electron diffraction [32]. Figures 5(a) and 5(b) exhibit the SAED patterns at RT along the respective $[01\bar{1}]$ and $[001]$ projections of the reported RT hexagonal lattice of $P\bar{3}m1$; all the observed reflections nicely correspond to the hexagonal symmetry, thereby affirming the RT structure. At 100 K (the lowest achievable temperature obtained using our electron-microscopy apparatus), additional reflections remarkably appear in Fig. 5(c) as compared to the RT counterpart of Fig. 5(a) and are reminiscent of superlattices relevant to a CDW onset. In principle, CDWs denote a sinusoidal charge-lattice modulation of the underlying periodicity; consequently, the superperiodicity of CDWs could be incommensurate or commensurate [33], for which a fractional superperiodicity is consistently forbidden due to an accompanied incomplete modulation [34,35]. In Fig. 5(e), a close inspection of the additional reflections in Fig. 5(c) (e.g., those in the red-dashed rectangle) shows ever existing intensities of the spots, whereas, if indeed CDWs, the associated high-order harmonics like that at $2c^*$ would signify a fractional modulation of $2/5$ of the superperiodicity and readily feature a vanishing intensity due to the correlated forbidden reflection [34,35]. The persistence of these additional spots in Figs. 5(c) and 5(e) rejects their origin as a CDW phase transition; all the spots in Figs. 5(c), 5(d), and 5(f) profoundly agree with the x-ray refined structure of triclinic $P\bar{1}$ in Table

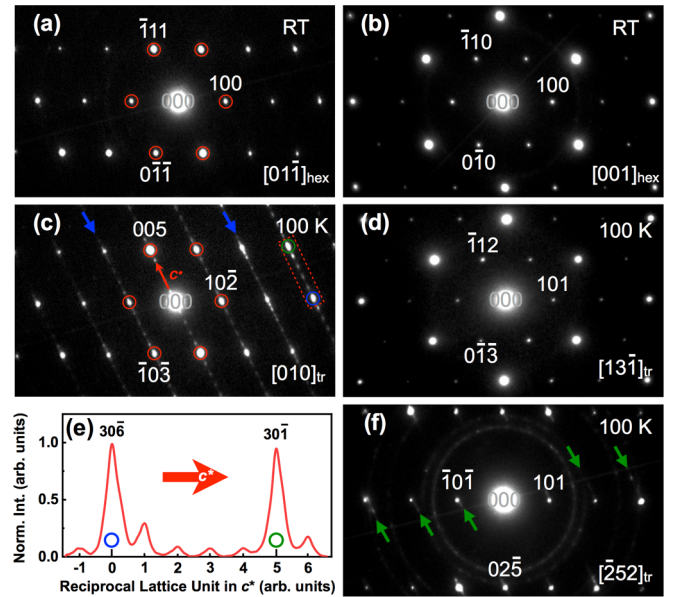


FIG. 5. SAED patterns of polycrystalline CuIr_2Te_4 acquired at room temperature along (a) $[01\bar{1}]$ and (b) $[001]$ zone axes in hexagonal (“hex”) $P\bar{3}m1$ and at 100 K along (c) $[010]$, (d) $[13\bar{1}]$, and (f) $[\bar{2}52]$ zone axes in triclinic (“tr”) $P\bar{1}$ structures derived by using Rietveld refinement. Red-circled spots in (a) can also be found in (c), though indexed differently owing to the structural phase transition from $P\bar{3}m1$ to $P\bar{1}$. (e) The intensity profile along the red-boxed c^* vector in (c), highlighting persistent reflections between the $30\bar{1}$ and $30\bar{6}$ spots. The extra spots along the blue arrows in (c) and polycrystalline rings in (f) are due to neighboring grains and those along green arrows in (f) are projected from the high-order Laue zone.

S1 [27], with the corresponding indexing being also indicated. Below T_s , CuIr_2Te_4 unambiguously transforms into the lower-symmetry structure with longer b and c axes as described in Table S1 [27]; consequently, it becomes free from a CDW modulation. The additional spots indicated by blue arrows in Fig. 5(c) and the polycrystalline rings in Fig. 5(f) arise from the contribution of nearby overlapping grains. Owing to the large cell dimension of the $P\bar{1}$ phase, projections from the high-order Laue zone are also observed [green arrows in Fig. 5(f)].

E. Temperature-dependent XANES and EXAFS measurements

To further support the first-order structural phase transition and exclude possible CDW at high T , we performed a complementary XANES and EXAFS measurements with respect to temperature, as shown in Fig. 6. XANES and EXAFS are powerful tools to determine the valence states and element-specific local structures. CDW formation is expected to cause a local-electronic-state instability, which reflects changes in the XANES and/or EXAFS. The RT XANES curves at the Cu K edge of CuIr_2Te_4 , Cu foil (Cu^0), Cu_2O (Cu^{1+}), and CuO (Cu^{2+}) are displayed in Fig. 6(a) for comparison. As per the quantitative analysis detailed in Fig. 7, the Cu valence in CuIr_2Te_4 at 300 K is close to $1+$. With T decreasing to 50 K, the absence of any spectral change suggests that the Cu valence of $1+$ persists in the low- T triclinic phase. Additionally,

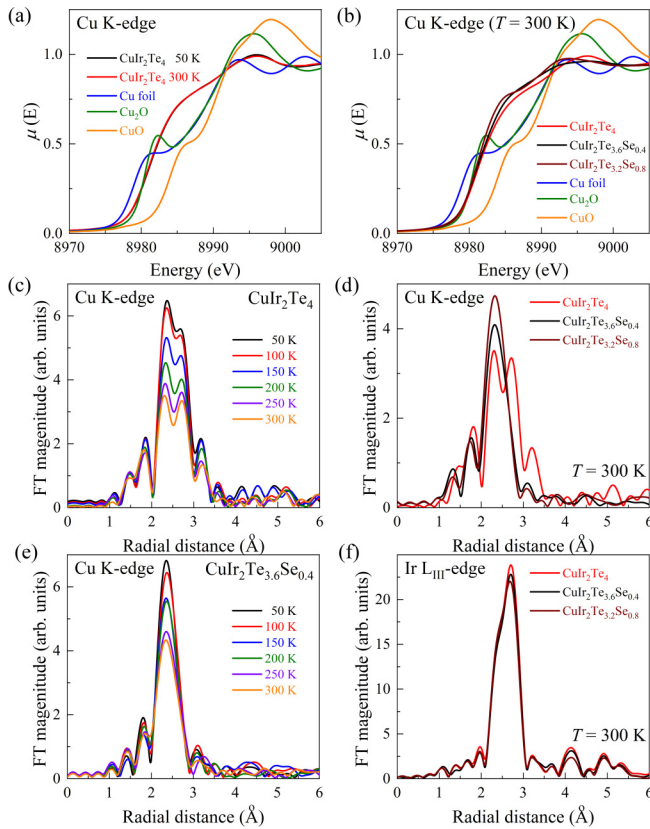


FIG. 6. XANES spectra at Cu K edge for $x = 0$ at (a) selected T values of 50 and 300 K and (b) $x = 0.1$ and 0.2 at 300 K. EXAFS spectra at Cu K edge for (c) $x = 0$ and (e) $x = 0.1$ from 50 to 300 K. EXAFS at (d) Cu K edge and (f) Ir L_{III} edge for $x = 0, 0.1,$ and 0.2 .

the RT XANES spectra corresponding to $x = 0, 0.1,$ and 0.2 shown in Fig. 6(b) indicate that Se doping does not afford a substantial Cu valence. For determining a local structure below/above T_s in CuIr_2Te_4 , we acquired the T -dependent EXAFS of CuIr_2Te_4 [Fig. 6(c)]. At 300 K, the radial distribution function (RDF) from EXAFS at the Cu K edge exhibits two features between 2 and 3 Å. In general, these results suggest two inequivalent bond lengths between Cu and the nearest Te in the local structure. When T decreases to 50 K, the two features gradually merge. The higher symmetry states of the eight identical Cu-Te bond lengths manifest a low- T triclinic phase that is stabilized with decreasing temperature. Subsequently, upon Se doping, only one main peak (indicating one Cu-Te bond length) is observed as per the RDF at 300 K. Therefore, Se doping forms a local structure with high symmetry at 300 K in Se-doped CuIr_2Te_4 [Fig. 6(d)]; this is similar to the effect of low T on CuIr_2Te_4 . In Fig. 6(e), the peak becomes sharper as T decreases, indicating that the low- T triclinic phase indeed contributes to the stabilization of the local Cu structure. Figure 6(f) shows the RT-EXAFS at the Ir L_{III} edge for $x = 0, 0.1,$ and 0.2 . The main feature in the Ir L_{III} edge RDF

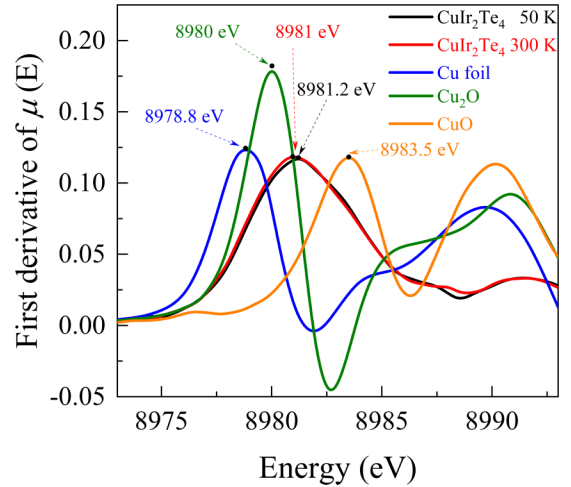


FIG. 7. Inflection points of the Cu K edge spectra in Fig. 6(a) are shown to determine the valence state of Cu. The analysis suggests that the valence of Cu in CuIr_2Te_4 is close to $1+$, although a slightly mixed valence cannot be excluded.

remains unchanged up to $x = 0.2$. These spectroscopic analyses demonstrate the local electronic stability of Cu and Ir.

IV. CONCLUSION

In summary, we have investigated the detailed structural, magnetic, transport, and spectroscopic properties of triangular-lattice CuIr_2Te_4 under ambient and pressurized conditions. We draw the following conclusions: (1) P application and chemical substitution (Se doping) significantly enhance T_s and suppress T_c , thus indicating that the high- T anomalous phase transition in CuIr_2Te_4 is inconsistent with the commonly speculated CDW formation. (2) P application and Se doping stabilize the low- T triclinic phase, as supported by *ab initio* calculations. (3) The Rietveld-refined SXRPD and SAED further confirm that the origin of the anomalous phase transition at T_s , which exhibits a large thermal hysteresis in the electrical resistivity and magnetization measurements, is the structural phase transition from the high- T hexagonal phase ($P\bar{3}m1$) to the low- T triclinic phase ($P\bar{1}$) and not CDW. (4) The spectroscopic XANES and EXAFS measurements of $\text{CuIr}_2(\text{Te}_{1-x}\text{Se}_x)_4$ show the stability of the local electronic structure, which largely reduces the possibility of CDW instability in CuIr_2Te_4 .

ACKNOWLEDGMENTS

This work was supported by the Ministry of Science and Technology, Taiwan, under Grants No. MOST 109-2112-M-110-019, No. MOST 108-2112-M-110-014-MY2, and No. 109-2112-M-009-012-MY3. Technical help from W. T. Huang is appreciated.

[1] M.-H. Whangbo, E. Canadell, P. Foury, and J.-P. Pouget, *Science* **252**, 96 (1991).

[2] X. Zhu, Y. Cao, J. Zhang, E. W. Plummer, and J. Guo, *Proc. Natl. Acad. Sci. USA* **112**, 2367 (2015).

- [3] K. Tsutsumi, T. Takagaki, M. Yamamoto, Y. Shiozaki, M. Ido, T. Sambongi, K. Yamaya, and Y. Abe, *Phys. Rev. Lett.* **39**, 1675 (1977).
- [4] J. Schäfer, E. Rotenberg, S. D. Kevan, P. Blaha, R. Claessen, and R. E. Thorne, *Phys. Rev. Lett.* **87**, 196403 (2001).
- [5] K. Zhang, X. Liu, H. Zhang, K. Deng, M. Yan, W. Yao, M. Zheng, E. F. Schwier, K. Shimada, J. D. Denlinger, Y. Wu, W. Duan, and S. Zhou, *Phys. Rev. Lett.* **121**, 206402 (2018).
- [6] B. Sipos, A. F. Kusmartseva, A. Akrap, H. Berger, L. Forró, and E. Tutis, *Nat. Mater.* **7**, 960 (2008).
- [7] K. K. Kolincio, M. Roman, M. J. Winiarski, J. Strychalska-Nowak, and T. Klimczuk, *Phys. Rev. B* **95**, 235156 (2017).
- [8] R. N. Shelton, L. S. Hausermann-Berg, P. Klavins, H. D. Yang, M. S. Anderson, and C. A. Swenson, *Phys. Rev. B* **34**, 4590 (1986).
- [9] K. Maiti, R. S. Singh, V. R. R. Medicherla, S. Rayaprol, and E. V. Sampathkumaran, *Phys. Rev. Lett.* **95**, 016404 (2005).
- [10] M. Bonilla, S. Kolekar, Y. Ma, H. C. Diaz, V. Kalappattil, R. Das, T. Eggers, H. R. Gutierrez, M.-H. Phan, and M. Batzill, *Nat. Nanotechnol.* **13**, 289 (2018).
- [11] B. Shen, F. Du, R. Li, A. Thamizhavel, M. Smidman, Z. Y. Nie, S. S. Luo, T. Le, Z. Hossain, and H. Q. Yuan, *Phys. Rev. B* **101**, 144501 (2020).
- [12] J. J. Yang, Y. J. Choi, Y. S. Oh, A. Hogan, Y. Horibe, K. Kim, B. I. Min, and S.-W. Cheong, *Phys. Rev. Lett.* **108**, 116402 (2012).
- [13] M. Kamitani, M. S. Bahramy, R. Arita, S. Seki, T. Arima, Y. Tokura, and S. Ishiwata, *Phys. Rev. B* **87**, 180501(R) (2013).
- [14] C. M. Tseng, C. H. Chen, and H. D. Yang, *Phys. Rev. B* **77**, 155131 (2008).
- [15] M. H. Lee, C. H. Chen, C. M. Tseng, C. S. Lue, Y. K. Kuo, H. D. Yang, and M.-W. Chu, *Phys. Rev. B* **89**, 195142 (2014).
- [16] M. H. Lee, C. H. Chen, M.-W. Chu, C. S. Lue, and Y. K. Kuo, *Phys. Rev. B* **83**, 155121 (2011).
- [17] C. S. Lue, Y.-K. Kuo, F. H. Hsu, H. H. Li, H. D. Yang, P. S. Fodor, and L. E. Wenger, *Phys. Rev. B* **66**, 033101 (2002).
- [18] D. Yan, Y. Zeng, G. Wang, Y. Liu, J. Yin, T.-R. Chang, H. Lin, M. Wang, J. Ma, S. Jia, D.-X. Yao, and H. Luo, [arXiv:1908.05438](https://arxiv.org/abs/1908.05438).
- [19] D. Yan, L. Zeng, Y. Lin, J. Yin, Y. He, X. Zhang, M. Huang, B. Shen, M. Wang, Y. Wang, D. Yao, and H. Luo, *Phys. Rev. B* **100**, 174504 (2019).
- [20] P. G. Radaelli, Y. Horibe, M. J. Gutmann, H. Ishibashi, C. H. Chen, R. M. Ibberson, Y. Koyama, Y.-S. Hor, V. Kiryukhin, and S.-W. Cheong, *Nature (London)* **416**, 155 (2002).
- [21] K. Takubo, S. Hirata, J.-Y. Son, J. W. Quilty, T. Mizokawa, N. Matsumoto, and S. Nagata, *Phys. Rev. Lett.* **95**, 246401 (2005).
- [22] D. I. Khomskii and T. Mizokawa, *Phys. Rev. Lett.* **94**, 156402 (2005).
- [23] H. Luo, T. Klimczuk, L. Muechler, L. Schoop, D. Hirai, M. K. Fuccillo, C. Felser, and R. J. Cava, *Phys. Rev. B* **87**, 214510 (2013).
- [24] M. Robbins, R. H. Willens, and R. C. Miller, *Solid State Commun.* **5**, 933 (1967).
- [25] K. Ohgushi, H. Gotou, T. Yagi, and Y. Ueda, *J. Phys. Soc. Jpn.* **75**, 023707 (2006).
- [26] S. Nagata, N. Matsumoto, R. Endoh, and N. Wada, *Physica B* **329-333**, 944 (2003).
- [27] See Supplemental Material at <http://link.aps.org/supplemental/10.1103/PhysRevB.103.104111> for information on the characterization of CuIr_2Te_4 .
- [28] L. Z. Deng, H. C. Wu, A. P. Litvinchuka, N. F. Q. Yuan, J. J. Lee, R. Dahal, H. Berger, H. D. Yang, and C. W. Chu, *Proc. Natl. Acad. Sci. USA* **117**, 8783 (2020).
- [29] H. D. Yang, P. Klavins, and R. N. Shelton, *Phys. Rev. B* **43**, 7681 (1991).
- [30] A. Ricci, N. Poccia, B. Joseph, L. Barba, G. Arrighetti, G. Ciasca, J.-Q. Yan, R. W. McCallum, T. A. Lograsso, N. D. Zhigadlo, J. Karpinski, and A. Bianconi, *Phys. Rev. B* **82**, 144507 (2010).
- [31] M. Tegel, S. Johansson, V. Weiß, I. Schellenberg, W. Hermes, R. Pöttgen, and D. Johrendt, *J. Phys.: Condens. Matter* **20**, 452201 (2008).
- [32] C. H. Chen, J. M. Gibson, and R. M. Fleming, *Phys. Rev. Lett.* **47**, 723 (1981).
- [33] W. L. McMillan, *Phys. Rev. B* **14**, 1496 (1976).
- [34] J. M. Tranquada, J. E. Lorenzo, D. J. Buttrey, and V. Sachan, *Phys. Rev. B* **52**, 3581 (1995).
- [35] J. M. Tranquada, J. D. Axe, N. Ichikawa, Y. Nakamura, S. Uchida, and B. Nachumi, *Phys. Rev. B* **54**, 7489 (1996).